# Assessment of current CFD performance prediction capabilities for novel rotor blade planforms.

**Thomas Fitzgibbon**
PhD student

**Mark Woodgate**
Research Associate

**George Barakos**
Professor

CFD Laboratory
University of Glasgow
Glasgow, UK

## ABSTRACT

This paper provides an assessment of modern CFD methods in predicting the rotor blade performance for advanced planform blade designs. The Langley BERP blade with an advanced tip shape is the primary supporting test case with results also presented for simpler blade designs such as the Langley Baseline and PSP rotor blade. The CFD method was able to achieve performance predictions of very good accuracy for all three blade designs in both hover and high-speed forward flight. However, further validation is required, for a blade with a more extensive experimental data set. The second part of the paper, focuses on analysis of the three rotor blade designs. In particular, typically used rotor efficiency metrics such as Figure of Merit and Lift to Drag ratio were only considered to be useful when comparing rotor designs at the same disk loading and operating conditions. The design analysis showed that subtle geometry features such as the blade thickness distribution across the blade tip and the exact blade planform shape can have a significant impact on the flow characteristics around advanced blade planforms showing the need for CFD coupled with optimisation methods.

## NOTATION

| | |
|---|---|
| $AR$ | aspect ratio |
| $c$ | rotor chord |
| $C_p$ | pressure coefficient |
| $C_f$ | skin friction coefficient |
| $C_q$ | blade section torque coefficient |
| $C_Q$ | torque coefficient |
| $C_t$ | blade section thrust coefficient |
| $C_T$ | thrust coefficient |
| $FoM$ | Figure of Merit |
| $L/D$ | Lift to drag ratio |
| $(L/D)_e$ | Equivalent lift to drag ratio |
| $N_b$ | Number of blades |
| $M$ | Mach number |
| $r$ | local radial position |
| $R$ | rotor radius |
| $\mathbf{R}$ | flow equation residual vector |
| $\mathbf{V}$ | flow equation cell volume |
| $\mathbf{W}$ | flow equation solution vector |
| $y^+$ | dimensionless wall distance |
| $\alpha_s$ | shaft angle |
| $\beta_0$ | coning angle |
| $\beta_{1s}, \beta_{1c}$ | flapping harmonics |
| $\mu$ | rotor advance ratio |
| $\psi$ | azimuthal angle |
| $\rho$ | density |
| $\sigma$ | rotor solidity |
| $\sigma_G$ | geometric rotor solidity |
| $\sigma_T$ | thrust-weighted rotor solidity |
| $\theta_0$ | collective angle |
| $\theta_{1s}, \theta_{1c}$ | pitching harmonics |
| $ref$ | reference |
| $i, j, k$ | cell index |
| $*$ | sonic |
| $\infty$ | freestream |

Presented at the Vertical Flight Society 75th Annual Forum & Technology Display, Philadelphia, Pennsylvania, May 13–16, 2019.


## INTRODUCTION

The advancement of rotor design is highly dependant on the accuracy of performance prediction tools. Accurate predictions lead to reduced uncertainties and give higher confidence in radical rotor designs. With the growth in computational power and development of CFD methods, improved rotor designs are likely to come from numerical simulation. In particular, the emergence of optimisation methods, allow to explore large design spaces, leading to significant potential performance benefits. Advanced planform shapes such as the BERP design (Ref. 1), Blue-Edge blade (Ref. 2) or new Boeing rotor blade (Ref. 3), show that rotor design is still progressing, and that the optimum rotor blade planform is still unknown. The differences in these designs also come from different aircraft sizes, mission requirements, and level of compromises

made between hover and forward flight conditions. As a first step, performance predictions for advanced planforms must be evaluated using modern CFD methods. The assumptions made by comprehensive rotor codes such as CAMRAD or HOST may lead to an inaccurate representation of the flow around more complex shapes. These tools to not capture the formation, roll-up and convection of the tip vortex and employ correction factors for three-dimensional aerodynamics, flow separation and viscous effects. These empirical correction factors may introduce significant errors for advanced rotor blade performance predictions, when the planform geometric features lead to non-negligible spanwise flow components inboard of the blade tip, as well as changes in flow field physics such as blade stall development mechanisms. Based on these observations, high fidelity CFD tools must be used for aerodynamic simulations of advanced rotor blade planforms. One of the main aims of new rotor designs is flight envelope expansion whether in lifting capability or maximum forward flight speed. This is achieved by minimizing the power required in conditions where it is close to the maximum power available. These correspond to hover at max weight and high-speed forward flight. The aim of this paper is to evaluate CFD predictive capabilities for more advanced planform shapes at these two critical flight conditions.

For this purpose, we use the experimental data of Yeager et al. (Ref. 4). To our knowledge, this is the only experiment concerning an advanced planform shapes in the public domain. Two rotor blades were tested here, a rectangular planform and a advanced planform with a paddle-shaped blade tip. Both blades were simulated in this paper using the HMB3 solver of Glasgow University in hover and high-speed forward flight condition. However, only integrated loads experimental data is available for these blades. For this reason, the PSP rotor blade (Ref. 5) is also simulated due to available surface pressure data. CFD validation is performed for these three blade designs by comparing the numerical predictions with available experimental data. The second part of the paper is focused on comparison of the three blade designs trimmed to a prescribed thrust coefficient in both hover and forward flight. In hover, the effect of anhedral on the rotor blade performance is examined for the Langley BERP and Baseline blades.

## CFD METHOD

The Helicopter Multi-Block (HMB3) (Refs. 6, 7) code of Glasgow University is used within this study. The HMB3 code solves the Unsteady Reynolds Averaged Navier-Stokes (URANS) equations in integral form using the Arbitrary Lagrangian Eulerian (ALE) formulation for time-dependent domains, which may include moving boundaries. The Navier-Stokes equations are discretised using a cell-centred finite volume approach on a multi-block structured grid. The spatial discretisation of these equations leads to a set of ordinary differential equations in time,

$$\frac{d}{dt}(\mathbf{W}_{i,j,k}\, V_{i,j,k}) = -\mathbf{R}_{i,j,k}(\mathbf{W}) \qquad (1)$$

where $i, j, k$ represent the cell index, $\mathbf{W}$ and $\mathbf{R}$ are the vector of conservative flow variables and flux residual respectively, and $V_{i,j,k}$ is the volume of the cell $i, j, k$. To evaluate the convective fluxes, the Osher (Ref. 8) approximate Riemann solver is used, while the viscous terms are discretised using a second order central differencing spatial discretisation. The Monotone Upstream-centred Schemes for Conservation Laws, which is referred to in the literature as the MUSCL approach and developed by Leer (Ref. 9), is used to provide high-order accuracy in space. The HMB solver uses the alternative form of the Albada limiter (Ref. 10) activated in regions where a large gradients are encountered mainly due to shock waves, avoiding non-physical spurious oscillations. An implicit dual-time stepping method is employed to perform the temporal integration, where the solution is marching in pseudo-time iterations to achieve fast convergence, which is solved using a first-order backward difference. The linearised system of equations is solved using the Generalised Conjugate Gradient method with a Block Incomplete Lower-Upper (BILU) factorisation as a pre-conditioner (Ref. 11). To allow an easy sharing of the calculation load on parallel computers, multi-block structured meshes are used (Ref. 12).

## BLADE GEOMETRIES

Three blade planforms, shown in figure 1 are the subject of this study: the Langley Baseline blade (LBL) with a rectangular planform, the Langley BERP blade (LBERP) with a paddle-shaped tip and the PSP blade with a swept-tapered blade tip.

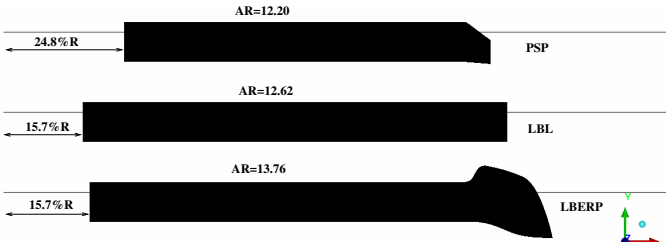


**Fig. 1. Planform geometries of the Langley Baseline, Langley BERP and PSP blades scaled to a chord of 1.0.**

The Langley BERP and Baseline blades were tested by Yeager et al. (Ref. 4) at model scale in a Freon-12 medium with a higher density than air. This allowed tests closer to full scale Reynolds numbers. The two blades tested have the same radius, aerofoils and twist distribution. Both blades have a linear twist of approximately -9 degrees, with a constant blade twist outboards of 0.866R. A RC(4)-10 aerofoil section is used inboards up to 0.84R, whereas the tip section used from 0.866R is the RC(3)-07 aerofoil. The aerodynamics of these two aerofoils are described by Noonan (Ref. 13), (Ref. 14). A linear transition was assumed between the two aerofoil sections. The main difference between the two blades is in the blade tip shape. The chord of the blade with the rectangular planform, referred to as the Langley Baseline blade (LBL) is also increased by 9% compared to the Langley BERP blade (LBERP) with the paddle shaped blade tip. This was done to

match the thrust weighted solidities of the two blades, leading to slightly different aspect ratios of the two blades (13.76 for LBERP and 12.62 for LBL). Based on the discussion between Perry and Amer (Refs. 15, 16), the matching of thrust weighted solidity may favour the LBL blade, due to higher geometric solidity (0.101 for LBL compared to 0.096 for the LBERP blade). The definition of thrust-weighted solidity does not account for three dimensional effects at the blade tip, hence reducing the planform effectiveness. Therefore, the direct comparison of performance between these two blades may not be valid (and other blades with equal thrust-weighted solidity. Furthermore, even though the thrust-weighted solidities are matched, the 9% chord increase for the LBL blade would lead to a higher blade weight penalty than that coming from the increased area of the LBERP blade tip. For the LBERP blade, a number of geometric uncertainties exist such as the exact blade tip shape and thickness distribution across the blade tip. The RC(3)-07 aerofoil was used up to 0.945R and then the thickness was tapered off linearly to an assumed trailing edge thickness of 0.04% c. The PSP rotor blade was also tested at model scale by Wong et al. (Ref. 5), and has fewer geometric uncertainties than the Langley BERP blade. This rotor blade has a linear blade twist of -14 degrees and a geometric solidity of 0.1033. The blade planform was generated using three radial stations. First, the RC(4)-12 aerofoil was used up to 65% $R$. Then, the RC(4)-10 aerofoil from 70% $R$ to 80% $R$. Finally, the RC(6)-08 aerofoil was used from 85% R to the tip. The planform of the PSP model rotor has a 60% tapered and 30° swept tip.

## COMPUTATIONAL SETUP

For all cases, the Chimera meshing technique was used, and the flow field was computed for isolated rotors. The boundary layer was assumed to be fully turbulent, with the $k\omega$-SST turbulence model used to close the RANS equations and aeroelastic effects neglected. In hover, to minimize computational costs a steady-state approach was used. A quarter of the rotor disk was modelled, with periodic boundary conditions in the azimuthal direction. This assumption is valid if the wake generated by the rotor is assumed periodic and the blades do not experience deep stall. A source/sink model was used for the simulations with Froude boundary conditions imposed at the inflow and outflow. In forward flight, the full rotor disk with four blades was simulated as the flow is unsteady. A hub was also included in the computational domain and modelled as a generic ellipsoidal surface. In forward flight a matrix trimming method was used to achieve the target thrust coefficient while minimizing rolling and yawing moments, with the full description found in (Ref. 6). In hover grid sizes of 10-12 million cells are used, whereas grid sizes of 30-45 million cells are used for forward flight computations. The detailed mesh properties for each of the rotor blades are presented in table 1. For each of the foreground meshes a C-H topology was used, with a H-grid round the tip for the LBL and PSP blades and an O-grid for the rounded LBERP tip. A wall distance of $1.0 \times 10^{-5}$ $c_{ref}$ was used, which ensured a $y^+ < 1$.

**Table 1. Grid sizes in millions of cells for the simulated rotor blades in hover and forward flight. PC = points in chordwise direction, PN = points in blade normal direction, PS = point in spanwise direction, FMESH = foreground mesh, BMESH = background mesh, TMESH = total mesh.**

| Blade | PC × PN × PS | FMESH | BMESH | TMESH |
|---|---|---|---|---|
| PSP | 252 × 56 × 215 | 5.2M | 7.2M | 12.4M |
| PSP (FF) | 198 × 46 × 145 | 4 × 2.8M | 20M | 31.2M |
| LBL | 234 × 64 × 118 | 3.9M | 4.9M | 8.8M |
| LBL (FF) | 234 × 64 × 118 | 4 × 3.9M | 27.8M | 43.4M |
| LBERP | 222 × 66 × 185 | 4.6M | 4.9M | 9.5M |
| LBERP (FF) | 222 × 66 × 185 | 4 × 4.6M | 27.8M | 46.2M |

For our simulations, each of the blades is scaled to a root chord of 1, hence the LBL blade is simulated for a 9% lower radius compared to the LBERP blade. The two blades were tested at a blade tip Mach number of 0.628 with a Reynolds number (based on tip speed) of $2.51 \times 10^6$ for the BERP-like blade and $2.74 \times 10^6$ for the Baseline. The PSP rotor blade was simulated at a lower blade tip Mach number of 0.58 and Reynolds number, based on the reference blade chord $c_{ref}$ of 5.45 inches and on the blade-tip speed, was $1.94 \times 10^6$. The computed test cases are shown in table 2.

**Table 2. Computational cases in hover and forward flight for the LBERP, LBL and PSP blades.**

| Blade | Hover | Forward flight |
|---|---|---|
| **CFD Validation** | | |
| LBERP | $\theta_0 = 9 - 13.5^o$ | $\mu = 0.4, C_T = 0.0081$ |
| LBL | $\theta_0 = 9 - 13.5^o$ | $\mu = 0.4, C_T = 0.0081$ |
| PSP | $\theta_0 = 4 - 12^o$ | $\mu = 0.35, C_T = 0.004, 0.006, 0.008$ |
| **Design comparison** | | |
| LBERP<br>LBL<br>PSP | $C_T = 0.008$ | $\mu = 0.4, C_T = 0.0081$ |

The comparison of the blade designs is performed in a quantitative manner where possible, however, due to different blade solidities, disk loadings, and blade tip Mach numbers, a qualitative approach must be used in the majority of analysed results. The differences are shown in table 3. In fact, the thrust-weighted solidities are very close for the three designs. The highly loaded LBL and LBERP cases at $13.5^o$ collective are also considered within the design analysis.

**Table 3. Differences in the rotor designs geometric properties, permitting primarily qualitative results analysis.**

| Blade | $\sigma_G$ | $\sigma_T$ | AR | $M_{TIP}$ |
|---|---|---|---|---|
| PSP | 0.1033 | 0.100 | 12.2 | 0.580 |
| LBL | 0.101 | 0.101 | 12.62 | 0.628 |
| LBERP | 0.096 | 0.101 | 13.76 | 0.628 |

The geometric and thrust-weighted solidities are defined as follows: $\sigma_G = \int_0^1 \sigma(r)dr$, which is equal to $N_b/(\pi R/c)$ for a rectangular blade; $\sigma_T = 3\int_0^1 \sigma(r)r^2dr$.

## RESULTS - CFD VALIDATION

This section presents comparisons of the CFD predictions with experimental data. In hover, performance predictions are obtained for all three blade designs and compared with experimental data. In forward flight, integrated loads are only available for the Langley blades, however the surface pressure predictions on the advancing and retreating blades are presented for the PSP blade. The hover performance predictions and comparisons with experimental data for the three blades are shown in figures 2-3.

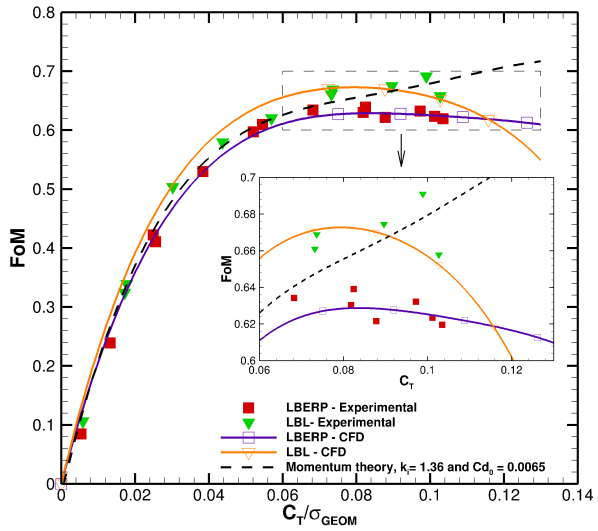


**Fig. 2. Hover performance predictions for the LBERP and LBL blades and comparisons with experimental data from Yeager et al. (Ref. 4).**

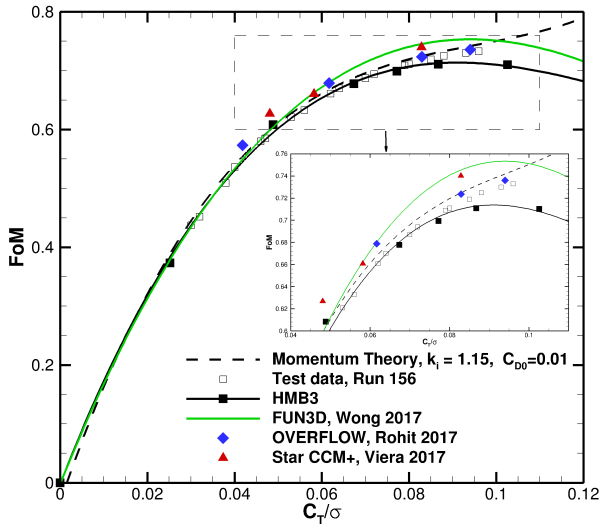


**Fig. 3. Hover performance predictions for the PSP rotor blade, and comparison with experimental data from Overmeyer and Martin (Ref. 17).**

The hover performance predictions show very good agreement with experimental data for all three simulated blades. For the LBERP and LBL blades, the CFD figure of merit curves fit well within the experimental data scatter. The main benefit of the LBERP blade is seen, where no significant performance loss can be observed at higher blade loading. At the highest collective, the performance of the LBERP blade surpasses the LBL blade. This is in agreement with literature (Ref. 1). The LBERP blade is able to operate at high loading conditions without major losses in thrust. The LBERP blade also has a lower geometric solidity when compared to the rectangular blade. As can be seen in the performance results, at each collective, the LBERP blade has a higher $C_T/\sigma$, which is especially visible at higher loading. Regarding the accuracy of the CFD results, it can be claimed that the use of the steady-state method is sufficient here, since no extensive stall is detected. The use of higher order numerical schemes or more advanced turbulent models could be justified when comparing with experimental data sets with fewer uncertainties. For the PSP blade, very good predictions are also obtained. Excellent agreement with experimental data can be seen for low and medium thrust levels, with a minor underprediction of approximately 2 counts in figure of merit at high thrust. This occurs as a result of modelling the rotor as isolated. The inclusion of the fuselage employed during experiments, improves the figure of merit by 1.4 counts when compared to an isolated rotor at $C_T/\sigma = 0.094$ (Ref. 18). This shows that modelling installation effects is important for accurate hover predictions, especially at high loading. Surface pressure predictions are also available for the PSP rotor blade at four thrust coefficients and were presented previously (Ref. 19). Unfortunately, no further data is available for advanced planform validation. For in-depth CFD validation, quantities such as surface pressure, sectional loads and vortex properties must be measured. Compensating errors may be present in the comparisons between CFD predictions and experimental data leading to a false sense of good agreement. The first step will be the future PSP tests in the large NASA NFAC wind tunnel facility, which will provide a comprehensive data set for CFD validation, however further testing is required for more advanced planforms.

The three blades are also simulated in high speed forward flight. Predictions of the integrated loads for the LBERP and LBL geometries are presented in table 4. Very good agreement can be seen for both blades with experimental data. The predicted performance of the LBERP blade is further away from experiment due to a higher degree of geometric uncertainty (Ref. 19). Aeroelastic effects may also be significant for the LBERP blade at high advance ratio, due to the advanced planform shape. Furthermore, the experimental trim states for these cases were unknown. Unfortunately, no further data is available for further validation of the CFD results. These results are analysed further in the section focused on rotor designs comparison.

For further validation of the CFD code for forward flight simulations, the PSP blade forward flight results are analysed at $\mu = 0.35$ and three thrust coefficient of $C_T$=0.004, 0.006 and 0.008. Integrated loads are not available for these case, however, surface pressure data was measured by Wong et

**Table 4. Integrated loads predictions for the Langley BERP and Baseline blades in forward flight and comparisons with experimental data from Yeager et al. (Ref. 4).**

| Blade | EXP- $C_Q$ | CFD - $C_Q$ | $\Delta\%$ |
|---|---|---|---|
| LBERP - $\mu$= 0.4 | $9.632 \times 10^{-4}$ | $9.396 \times 10^{-4}$ | -2.5% |
| LBL - $\mu$= 0.4 | $9.082 \times 10^{-4}$ | $9.049 \times 10^{-4}$ | -0.4% |

al. (Ref. 5). The surface pressure predictions for the advancing and retreating blade sides are shown in figure 4.

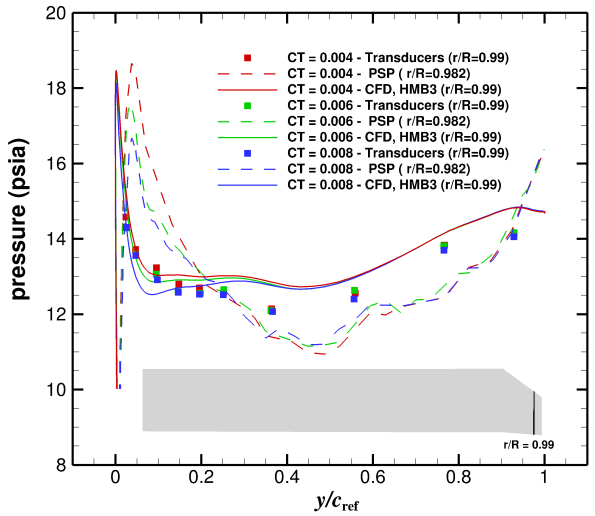


(a) Advancing blade side

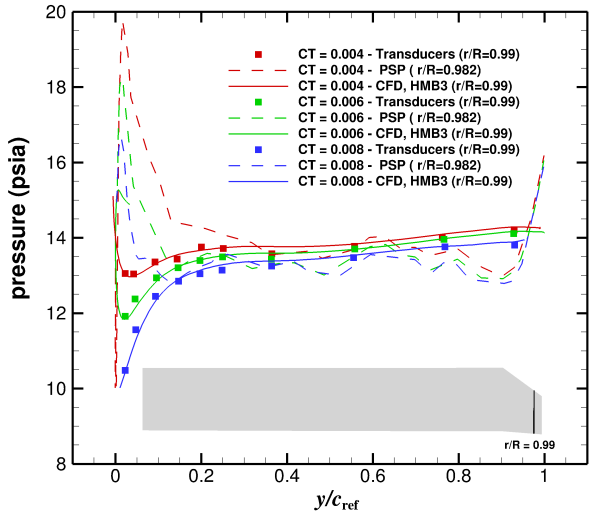


(b) Retreating blade side

**Fig. 4. Surface pressure predictions for the PSP blade in forward flight at three thrust levels. Comparisons are shown for the upper surface of the rotor at $r/R = 0.99$ for the advancing and retreating blade sides with experimental data from transducers and the PSP technique (Ref. 5).**

The CFD data agrees very well with the data from the pressure transducers. Excellent agreement is seen on the retreating blade side, whereas on the advancing side, the surface pressure is slightly overpredicted. The pressure transducers, do not however, resolve the suction peak, hence this key feature of the pressure distributions cannot be verified. The pressure sensitive paint data fails to capture the correct curve trends, which is especially visible on the retreating blade side, where the dynamic pressure is low. Some errors may occur due to the fact that the pressure using the PSP technique was extracted at $r/R = 0.982$, whereas the pressure transducers were installed at $r/R = 0.99$. Unfortunately, further experimental data for the PSP rotor blade in forward flight is unavailable.

## RESULTS - ROTOR DESIGN COMPARISON

The obtained CFD results are analysed further, from a rotor design perspective. The figure of merit values cannot be compared directly, due to different disk loading of the rotors. The figure of merit is written in terms of net thrust and power in equation 2

$$FoM = \frac{C_T^{3/2}}{\sqrt{2}C_Q} = \frac{T\sqrt{DL}}{P\sqrt{2\rho}} \tag{2}$$

where, DL (= T/A) is the rotor disk loading , T is the rotor thrust, P is the rotor power and A is the disk area.

Based on equation 2 rotors with a higher disk loading will achieve, higher values of figure of merit due to the 3/2 power factor of the thrust coefficient. However, for high rotor efficiency, high power loading is sought for, and is maximized by minimizing disk loading and maximizing figure of merit. The disk loading value, however, is usually set based on the vehicle class and sizing requirements. Furthermore, a higher solidity (geometric) rotor will lead to a shift in the maximum figure of merit value to higher thrust coefficients by delaying the onset of stall. For this reason, the solidity (in many cases thrust-weighted) of a rotor is constrained in many hover optimisation studies (Refs. 20–23), when the objective is to maximize the figure of merit. These statements lead to favourable treatment of the LBL blade compared to the LBERP blade, when directly comparing in terms of figure of merit. The PSP rotor operates and even lower disk loading, and has a higher rotor solidity. However, the main reason for the higher figure of merit for the PSP rotor when compared to the Langley blade designs, come from reduced compressibility effects due to the lower blade tip Mach number (0.58 compared to 0.628). Finally, due to the lower tip speed and rotor radius for a given thrust coefficient, the PSP rotor will produce a lower net thrust. Based on these observations, comparisons of the three blade designs is performed qualitatively. Firstly, the hover solutions are examined at $C_T = 0.008$ for the three blade designs, along with the high thrust cases (13.5 deg collective) for the Langley BERP and Baseline blades. The surface pressure distributions and skin friction lines are shown in figures 5-8.

The typical characteristics of the blade loading distribution across the blade tips for each blade design can be seen in the pressure coefficient distribution plots. For the LBERP tip, two regions of high suction exist, which are inboard of the notch

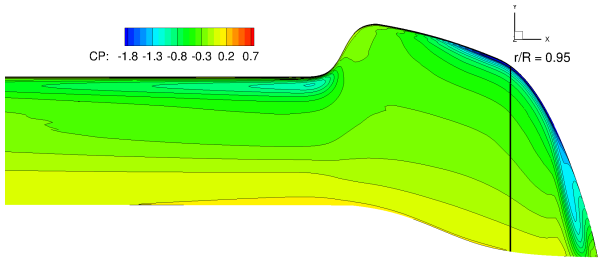


(a) LBERP

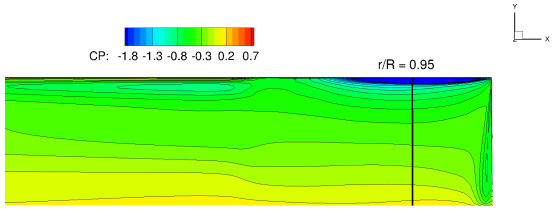


(b) LBL

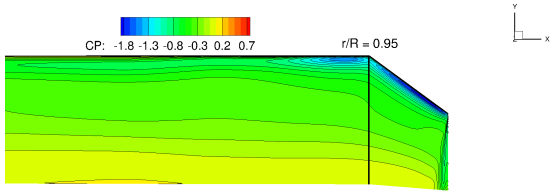


(c) PSP

**Fig. 5. Surface pressure coefficient distributions across the blade tip for the LBERP, LBL and PSP blade designs at $C_T$=0.008.**

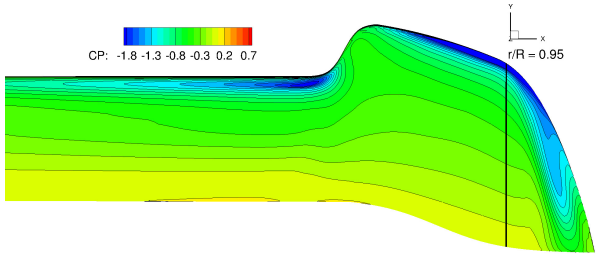


(a) LBERP

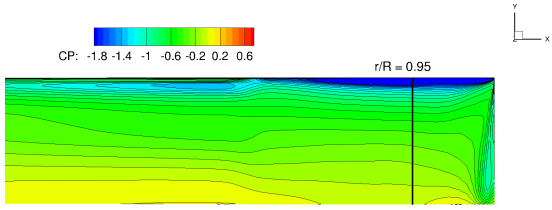


(b) LBL

**Fig. 6. Surface pressure coefficient distributions across the blade tip for the LBERP and LBL designs at 13.5 degrees collective.**

and round the swept tip. With increasing collective these suction regions grow and propagating inboard and covering a larger portion of the paddle-shape tip. The effect of the tip vortex is also clearly seen. The tip vortex separates inboards of the very tip of the blade, which is especially visible for the high collective case. This could be one of the causes for the poor performance of the Langley BERP blade, as the blade tip

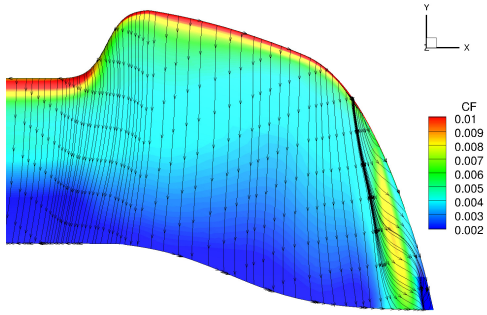


(a) LBERP

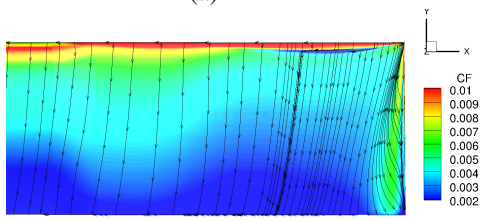


(b) LBL

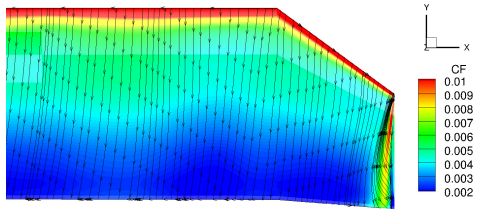


(c) PSP

**Fig. 7. Surface skin friction coefficient distributions and surface skin friction lines for the LBERP, LBL and PSP blade designs at $C_T$=0.008.**

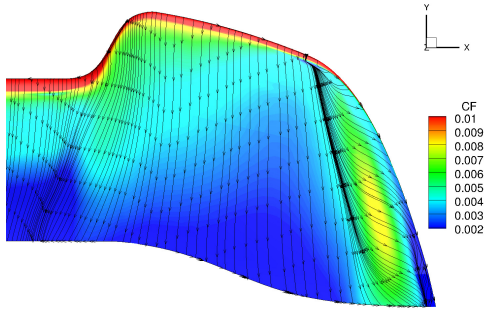


(a) LBERP

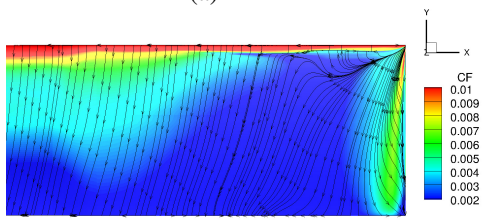


(b) LBL

**Fig. 8. Surface skin friction coefficient distributions and surface skin friction lines for the LBERP and LBL designs at 13.5 degrees collective.**

vortex is expected to form round the curve tip. Such behaviour of the tip vortex can be seen for the production BERP III and BERP IV blades based on the surface pressure distributions in hover (Euler computation) (Ref. 24). The early vortex separation for the LBERP blade is attributed to the too low blade thickness in this region. Tapering off the blade quadratically rather than linearly could potentially prevent this, leading to a more optimal blade thickness distribution. The pressure distribution for the rectangular Langley Baseline blade is typical of a rectangular blade design. A sharp suction peak can be seen near the leading edge at the tip of the blade which leads to decreased performance compared to more modern blade designs such as a design with a parabolic blade tip. The rapid aerofoil transition, causes a non-smooth pressure distribution, which can especially be seen in Figure 5 b). At the higher collective the pressure contours indicate the onset of separation across the blade tip, as the blade pressure is no longer recovered at the trailing edge. The PSP blade pressure contours, show the effect of sweeping the blade tip. A reduced suction is seen when compared to the rectangular blade, with the sweep onset acting as a aerodynamic discontinuity. The more favourable pressure contours, however, are also due to the lower blade tip Mach number. Further observations can be made based on the skin friction lines. For the LBERP blade, the skin friction lines at the very tip of the blade indicate the presence of the tip vortex. The tip vortex forms further inboard than for a typical BERP blade, as seen in the pressure distribution contours. At the higher thrust case, the vortex forms even further inboards. A different thickness distribution as well as leading edge curve outboard of 0.95R could greatly improve these surface streamline flow features, leading to formation of the tip vortex round the curved blade tip. Evidence of the notch vortex formation is also seen for the higher thrust case, as a drop in skin friction is seen. At higher thrust a low level of shock induced separation can be observed near the leading edge. The skin friction lines indicate much stronger separation for the LBL blade at high thrust. Significant separation is seen across the blade tip, with a weak separation also seen at $C_T = 0.008$. At high thrust, the pressure is no longer fully recovered at the trailing edge for the LBL blade, indicating the onset of stall. This is the primary reason for the lower performance of this blade at 13.5 degrees collective when compared to the Langley BERP design, which is able to operate at much higher collectives without developing stall. The flow over the tip of the PSP rotor blade is much cleaner as no shock induced separation is observed, which is also due to the lower blade tip Mach number, as stated previously. Unfortunately, a high collective case is unavailable for the PSP rotor blade for comparisons at high thrust. The chordwise surface pressure coefficients are examined further for the three blade designs at r/R = 0.95 and shown in figures 9-10. The critical pressure coefficients are also shown to indicate where the flow becomes supersonic.

The chordwise pressure coefficient distributions show that the comparison of different blade designs at a constant radial station is not fully valid. The key features of the blade pressure distribution are dependent on the planform shape, and may be

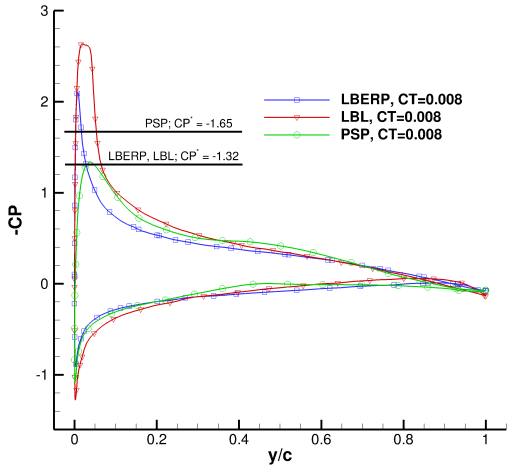


**Fig. 9. Chordwise surface pressure coefficient at r/R=0.95 for the LBERP, LBL and PSP blade designs at $C_T = 0.008$.**

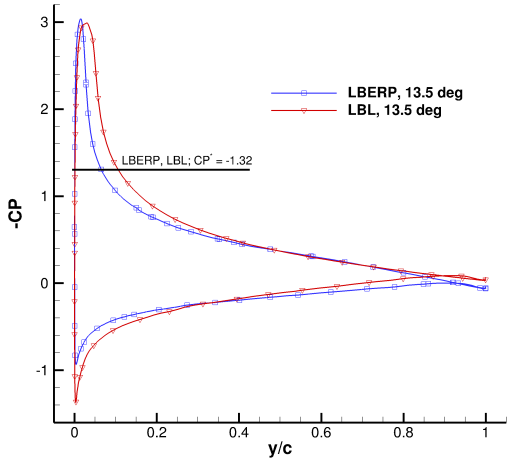


**Fig. 10. Chordwise surface pressure coefficient at r/R=0.95 for the LBERP and LBL designs at 13.5 degrees collective (high thrust case).**

located at different radial stations. For example at r/R = 0.95, a drop in the suction peak is observed for the PSP rotor blade, as this is the point of the sweep initiation. A region of higher suction is seen for the Langley BERP blade further inboard (r/R = 0.82) due to the notch geometry, which is not present for the straight PSP rotor blade. However, qualitative observations can be made based on the chordwise surface pressure at r/R = 0.95. At $C_T = 0.008$ it can be seen that the suction peak for the LBL blade is much higher than for the other two blades. This is due to sweep incorporated in the LBERP design. The LBERP blade has a sweep of only 9 degrees, however the blade loading is also distributed over a larger area due to the increased blade chord. These are also the reasons for reduced chordwise extent of supersonic flow when compared to the Langley Baseline blade. The flow over the PSP rotor blade at r/R = 0.95 is subsonic, as the suction peak is below the critical surface pressure coefficient. This is due to the lower blade tip Mach number when compared to the Langley blades. For the cases at 13.5 degrees collective, a similar suction peak magnitude can be observed for the LBL and LBERP

blades. However, at this collective, the LBERP blade operates at a much higher thrust coefficient. Once again, the supersonic flow region is reduced for the LBERP blade, when compared to the LBL blade. The pressure is not longer fully recovered for the LBL blade, indicating the onset of stall. The analysis of different blade designs is continued by extracting the sectional blade loads for the three blade designs at $C_T = 0.008$, shown in figures 11-12. The LBL loads are also shown scaled to the radius of the LBERP blade (1.09 factor). The loads are scaled by the local flow velocity and reference blade chord equal to the chord of the first aerodynamic section.

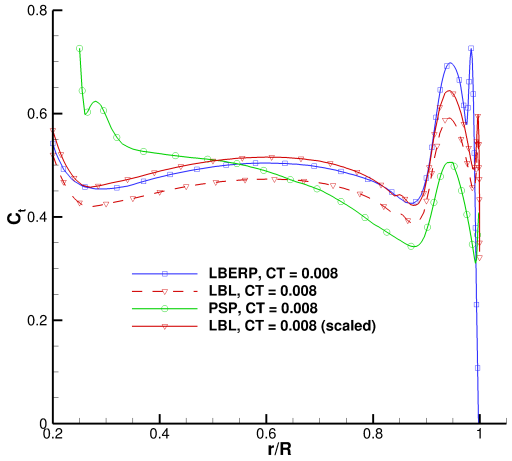


**Fig. 11. Sectional thrust distributions for the LBERP, LBL and PSP blade designs at $C_T = 0.008$. Loads are scaled by the local flow velocity and reference blade chord equal to the chord of the first aerodynamic section.**

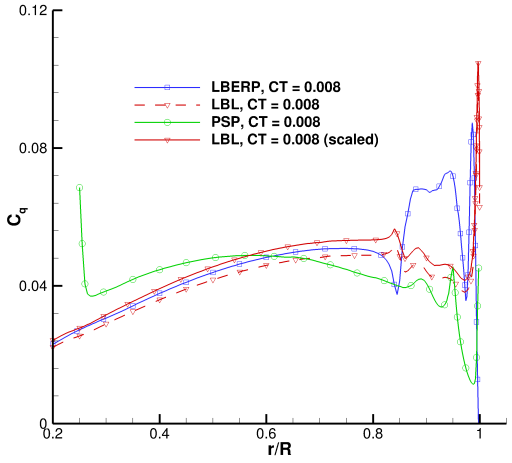


**Fig. 12. Sectional torque distributions for the LBERP, LBL and PSP blade designs at $C_T = 0.008$. Loads are scaled by the local flow velocity and reference blade chord equal to the chord of the first aerodynamic section.**

The sectional thrust distributions indicate a similar blade loading for the three blade designs. Due to the scaling by local flow velocity, the loading at the root of the blade is augmented. The two peaks in the blade loading are due to the formation of the tip vortex as well as the effect of the preceding blade tip vortex. The loading peak at the blade tip is higher for the LBERP blade when compared to the LBL blade, leading to reduced hover performance. This is due to the non-optimal thickness distribution across the tip of the blade. The PSP rotor blade has a much more optimal loading distribution compared to the Langley blades. However, this is also due to the higher blade twist of the blade (14 degrees compared to 9 degrees), as can be seen by the slope of the blade loading distribution curve. This leads to an offloading of the blade tip, and hence higher performance. The radial torque distributions show much greater differences. The LBERP blade geometry leads to a reduction in local torque at the notch, however, an increased torque is observed across the paddle type blade tip. A reduced peak is seen at the blade tip when compared to the LBL blade. The result of the aerofoil transition can also be seen for the LBL blade. A more uniformly distributed loading can once again be seen for the PSP blade. In particular, the swept blade tip leads to a significant drop in local torque. The tip vortex formation for the three blades is shown in figure 13.

Figure 13 shows the different tip vortex formations for the three blade designs. For the LBERP blade, the onset of the tip vortex is located close to the edge of the blade tip, further inboards than for the other two blade designs. The tip vortex grows around the curved tip, moving towards the upper surface near the trailing edge of the blade. A secondary tip vortex structure is present for a longer period for the LBERP blade compared to the other two blades. For the PSP and LBL blades, both blade tip vortices form on the upper surface close to the blade leading edge. The tip vortex for the PSP blade, however, travels a shorter distance before separating at the blade trailing edge due to the blade tip taper. The blade sweep also moves the vortex onset downstream along the chordwise direction. These features can have a significant effect on the loading at the blade tip and hence the rotor blade performance. Another solution for improving a blades hover performance is anhedral. This was studied for the Langley BERP and Baseline blades at 10.5 degrees collective, through applying 15 degrees parabolic anhedral initiated at 0.945R (the starting position of the LBERP raked tip). The performance improvement is shown in Table 5.

**Table 5. Hover performance of standard LBERP and LBL blades, and blades with 15 degrees parabolic anhedral.**

| Blade | $C_T$ | $C_Q$ | *FoM* | FoM % |
|---|---|---|---|---|
| LBL | 0.00885 | 0.000880 | 0.6702 | - |
| LBERP | 0.00882 | 0.000934 | 0.6276 | - |
| LBL (anh) | 0.00891 | 0.000849 | 0.6997 | +4.4% |
| LBERP (anh) | 0.00888 | 0.000883 | 0.6698 | +6.7% |

The tip anhedral increases the hover performance for both blades. For the Langley Baseline blade, a performance improvement of approximately 3 counts in figure of merit is achieved, whereas the Langley BERP blade sees an increase of over 4 counts. Therefore, it can be stated that blade anhedral is more beneficial for the Langley BERP geometry than the Baseline blade. The Langley BERP blade with 15 de-

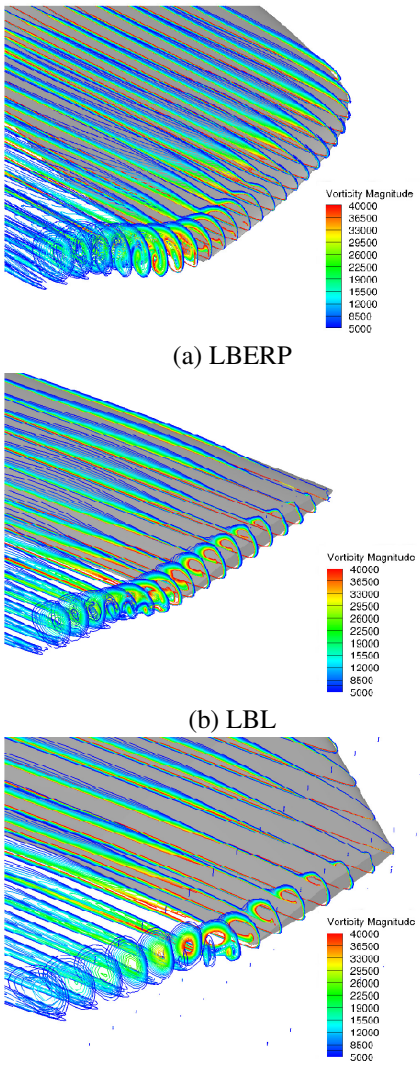


(a) LBERP

(b) LBL

(c) PSP

**Fig. 13. Vortex formation for the LBERP, LBL and PSP blade designs at $C_T$=0.008 based on contours of vorticity.**

grees achieved a similar figure of merit as for the standard Langley Baseline blade. The performance improvement due to anhedral, comes from a small increase in thrust and torque reduction. Of course, no experimental data exists to validate this results, however the benefit of blade anhedral is also seen for the S-76 rotor blade (Ref. 25). To examine the sources of the beneficial action of anhedral, the surface pressure distributions and sectional loads are compared. The surface pressure distribution for the Langley BERP and Baseline blades with and without anhedral are shown in Figure 14. The pressure coefficient is normalised by local flow velocity.

The anhedral is found to redistribute the loading along the blade leading to an offloading of the blade tip and higher loading inboard. This leads to a more optimal induced lift distribution and reduced overall torque. In fact, the blade anhedral acts similarly as additional negative twist on the blade loading distribution. The differences in blade loading for the blades with and without anhedral are noticeably lower for the Langley Baseline blade. The aerofoil transition region, can also

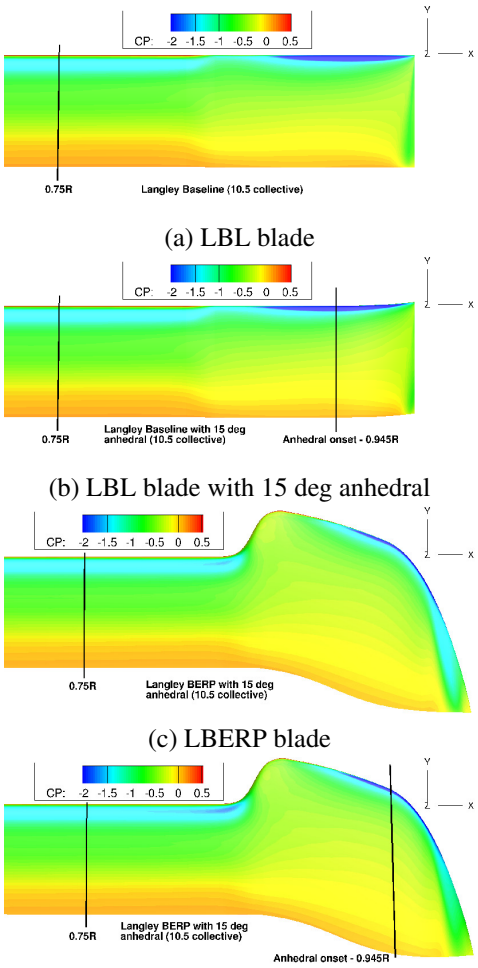


(a) LBL blade

(b) LBL blade with 15 deg anhedral

(c) LBERP blade

(d) LBERP blade with 15 deg anhedral

**Fig. 14. Comparison of the surface pressure distributions (normalised by local flow velocity) for the LBL and LBERP blades in hover with and without anhedral.**

be clearly seen in the surface pressure distributions, where the pressure iso-lines spread out. For the Langley BERP blade, a reduced suction at the blade tip can be observed (caused by formation of the tip vortex). The suction, however, is increased in the blade notch region. This is highlighted further through the sectional load distributions, in Figures 15. The loads are normalised by local flow velocity and the reference blade chord taken as the chord of the first aerodynamic section.

The observations from the surface pressure distributions are confirmed by the sectional load distributions. The anhedral has a similar effect on the rotor thrust distributions, where a larger amount of thrust is generated inboard. The benefit of anhedral, mainly comes from a reduction in torque at the blade tip, which is seen for both blades. For the Langley BERP tip, the largest reduction can be seen across the paddle-like blade tip, as well as at the very end of the tip where the tip vortex forms. For the Langley Baseline blade, the torque is reduced past the aerofoil transition region. To investigate the differences in blade loading, the vertical tip vortex displacements are extracted from the solutions and are shown in figure 16.

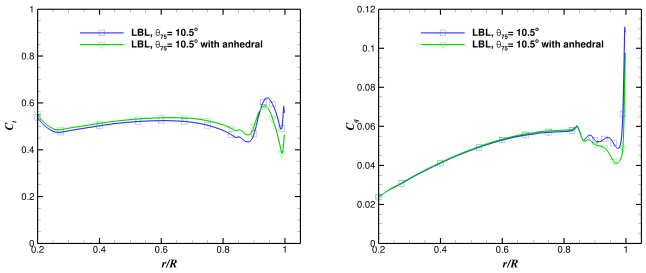


(a) LBL blade, $C_t$ (b) LBL blade, $C_q$

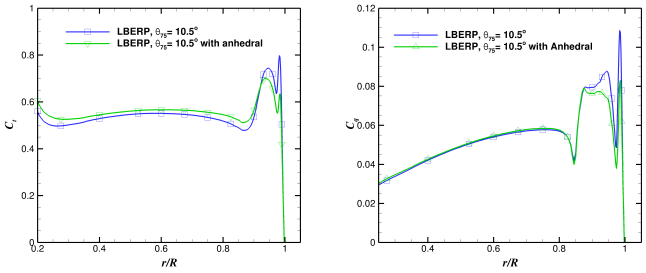


(c) LBERP blade, $C_t$ (d) LBERP blade, $C_q$

**Fig. 15. Comparison of sectional thrust and torque distributions for the LBL and LBERP blades in hover with and without anhedral.**

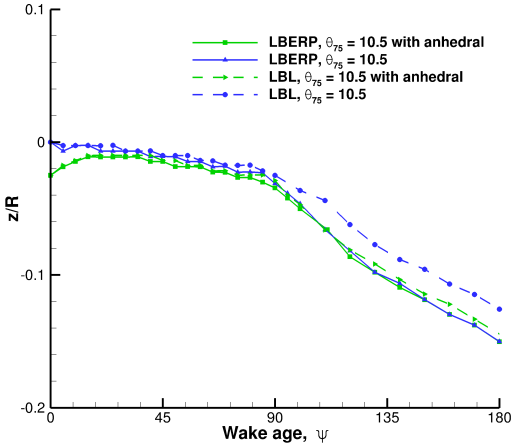


**Fig. 16. Comparison of the tip vertical vortex displacements for the LBL and LBERP blades in hover with and without anhedral.**

The vertical tip vortex displacements indicate that for the blades with anhedral, so called "vortex snaking" occurs, as the tip vortex initially moves upwards, before displacing downwards. This behaviour was also observed by Brocklehurst and Barakos (Ref. 26). The typical change in the gradient of vortex descent is seen as the vortex passes the next blade at 90 degrees azimuth. The vertical miss distance is marginally higher for the blades with anhedral, however this effect is not seen to be significant. In the later wake ages, the vortex is displacement is similar for all blades, except for the LBL blade without anhedral which displaces at a slower rate. At this collective, the LBL blade produces a weaker downwash field near the blade tip compared to the LBERP blade. This also leads to a reduced effect on the tip vortex vertical displacements due to the introduction of anhedral. The vortex strength due to the introduction of anhedral is examined next, and is shown in figure 17.

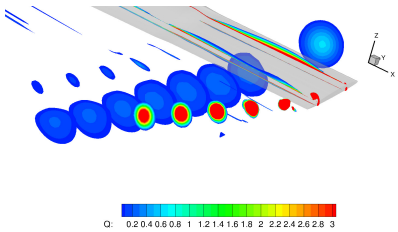

(a) LBL blade

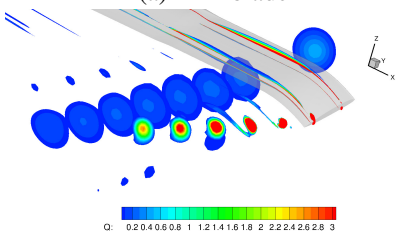

(b) LBL blade with anhedral

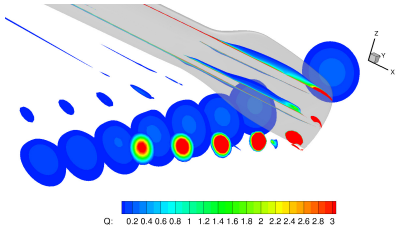

(c) LBERP blade

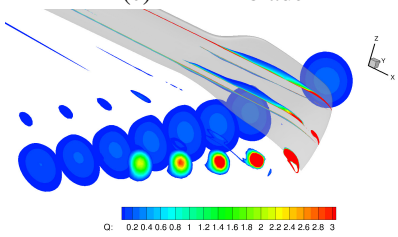

(d) LBERP blade with anhedral

**Fig. 17. Comparison of vortex strength for the Langley blades with and without anhedral as indicated by a Q-criterion contour at various aziumthal locations. A cutoff below Q=0.02 is applied.**

For both blade designs, the addition of anhedral leads to a weaker tip vortex. The LBERP blade generates a weaker blade tip vortex at this collective, despite operating at a higher thrust coefficient. The vortex radius before interacting with the next blade is also clearly larger for the LBERP blade when compared to the LBL blade. Based on these observations, it can be seen that the LBERP tip vortex aerodynamics are favourable compared to the LBL blade, and the addition of anhedral further offloads the blade tip. The effects of anhedral also show that advanced planforms require careful computational optimisation. This is due to the strong sensitivity of geometric features such as anhedral on the blade performance, as shown for the Langley Baseline and BERP blades.

Further analysis is performed by examining the LBERP, LBL and PSP blades in high-speed forward flight. The three blades were simulated at the same advance ratio of 0.4 and trimmed to the same thrust coefficient of 0.0081 (whilst minimizing pitching and rolling moments). The obtained trim states are shown in table 6.

**Table 6. Trim states for the forward flight computations of the LBERP, LBL and PSP blades at $\mu = 0.4$ and $C_T = 0.0081$. Values all given in degrees.**

| Blade | LBERP | LBL | PSP |
|---|---|---|---|
| $\alpha_s$ | -7.449 | -7.449 | -6.0 |
| $\theta_0$ | 12.920 | 12.535 | 11.124 |
| $\theta_{1s}$ | 10.891 | 10.437 | 9.229 |
| $\theta_{1c}$ | -4.229 | -4.022 | -3.336 |
| $\beta_0$ | 3.43 | 3.43 | 3.5 |
| $\beta_{1s}$ | -1.0 | -1.0 | 0.0 |
| $\beta_{1c}$ | -0.7 | -0.7 | 0.0 |

The trim states, indicate a lower collective and longitudinal cyclic angles for the PSP rotor blade when compared to the Langley blades. This is due to the fact that this rotor produces a lower net thrust for a given thrust coefficient (due to a lower rotor radius and blade tip Mach number). The matching of thrust-weighted solidity, which led to an increase in 9% chord for the LBL blade, leads to a slightly lower collective and longitudinal cyclic compared to the LBERP blade. The shaft, flapping and coning angles are prescribed.

As mentioned previously, rotor designs in hover are typically compared in terms of figure of merit. In forward flight, the aerodynamic efficiency measure often used is the lift to drag ratio (L/D), shown in equation 3.

$$\frac{L}{D} = \frac{WV_\infty}{P} = \frac{C_L}{C_Q}\mu \tag{3}$$

where W is the weight of the helicopter, $V_\infty$ is the flight speed and P is the rotor power, and $\mu$ is the rotor advance ratio.

In rotorcraft this parameter is proportional to the power loading and flight speed of the helicopter. Rotors with high disk loading will generally have a lower power loading, and hence lower lift to drag ratio. Therefore, this parameter will favour rotor designs with low disk loading. The lift to drag ratio will decrease with increasing weight of the helicopter. Heavy-lift helicopters will generally have poor lift to drag ratios, however, may have a much wider flight envelope than lower loaded helicopters. Direct comparison of rotor designs in terms of lift to drag ratio is only valid for rotors with the same disk loading, as well as aircraft weight. Furthermore, this parameter does not directly account for differences in the generated propulsive force. For this reason, an equivalent lift to drag ratio, $(L/D)_e$, is also often used, defined in equation 4.

$$\left(\frac{L}{D}\right)_e = \frac{C_L}{C_Q/\mu - C_D} \tag{4}$$

where $C_D$ is the drag coefficient which is equal to the propulsive force coefficient (assumed trim).

The calculated lift to drag ratios, as well as equivalent lift-to-drag ratios when scaled two different full-scale helicopter rotors (UH-60A and AH-64) are shown in table 7.

**Table 7. Comparison of various lift-to-drag ratio values for the LBERP, LBL and PSP rotor designs at $C_T = 0.0081$ and $\mu = 0.4$. Same propulsive force coefficient assumed for the AH-64 and UH-60A helicopters.**

| Blade | LBERP | LBL | PSP |
|---|---|---|---|
| $L/D$ | 3.45 | 3.58 | 4.34 |
| $(L/D)_e$ (UH-60A) | 6.23 | 6.68 | 7.97 |
| $(L/D)_e$ (AH-64A) | 6.23 | 6.68 | 7.97 |

At a constant thrust coefficient of 0.0081, the PSP rotor blade generates 1.5 times less net thrust than the LBERP blade and 1.25 times less net thrust than the LBL blade due to the lower aspect ratio and lower blade tip Mach number. This leads to higher L/D ratio of the PSP rotor compared to the Langley blades. Similarly, the LBERP blade produces 1.18 more thrust, than the LBL blade for a given thrust coefficient. This is due to the fact, that the LBL blade chord was increased by 9% and the simulated blades were scaled to a chord of 1.0. The equivalent lift to drag ratios are calculated by scaling the model scale rotor blades to the full scale radius. The drag coefficient is calculated based on the prescribed shaft angle. Therefore, the propulsive force generated by the PSP rotor blade is lower than for the LBL and LBERP designs. The propulsive force required for the UH-60A and AH-64A helicopters was assumed as constant (although the equivalent flat plate areas will not be due to different rotor radii). The equivalent lift to drag ratio is the same for any helicopter as the value is only dependent on the rotor lift and torque and the required propulsive force. However, the Apache helicopter is operated at a higher disk loading, and hence for a given thrust coefficient, the weight of the aircraft will be lower. Here, at $C_T = 0.0081$, the UH-60A operates at 22,132lbs whereas the Apache rotor operates at 18,362lbs. In fact, the condition of $C_T = 0.0081$ and $\mu = 0.4$ is outside the flight envelopes of both helicopters. Based on these observations it can be stated, that the L/D and $(L/D)_e$ values may be misleading for different rotor designs. The rotors must be compared for the same helicopter weight and disk loading to gain valuable insight. For this reason, when comparing rotors operating at different conditions, moving to the dimensional form of forces and moments may be more valuable. However, despite considerably different net thrust values qualitative analysis of the three blade designs can be performed.

The rotor disk blade loads are extracted for the three blade designs and shown in figure 18. Note that the PSP blade loads are shown on a different scale compared to the Langley blades. As the LBL and LBERP blades were simulated at the same blade tip Mach number, the difference between these two blades is also shown. All loads are scaled by the reference blade chord (equal to the chord of the first aerodynamic section), and the pitching moments are taken about the local quarter chord location (chord taken as normal to pitch axis).

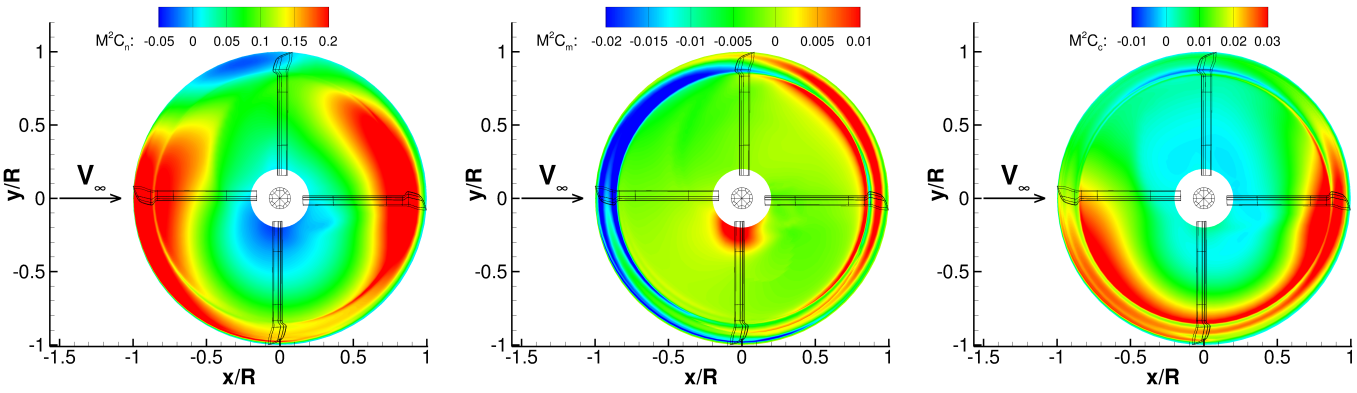


(a) LBERP, $M^2C_N$ (b) LBERP, $M^2C_M$ (c) LBERP, $M^2C_C$

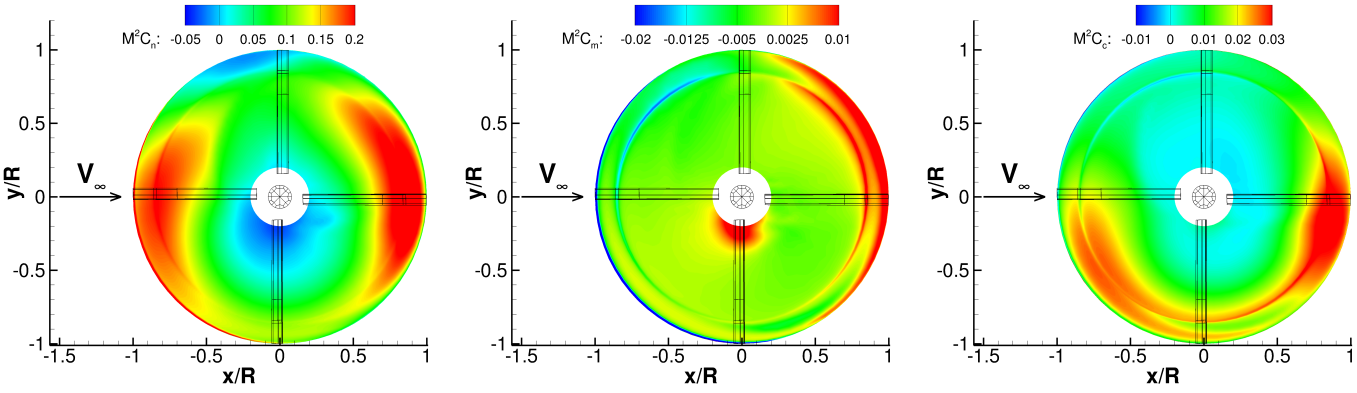


(d) LBL, $M^2C_N$ (e) LBL, $M^2C_M$ (f) LBL, $M^2C_C$

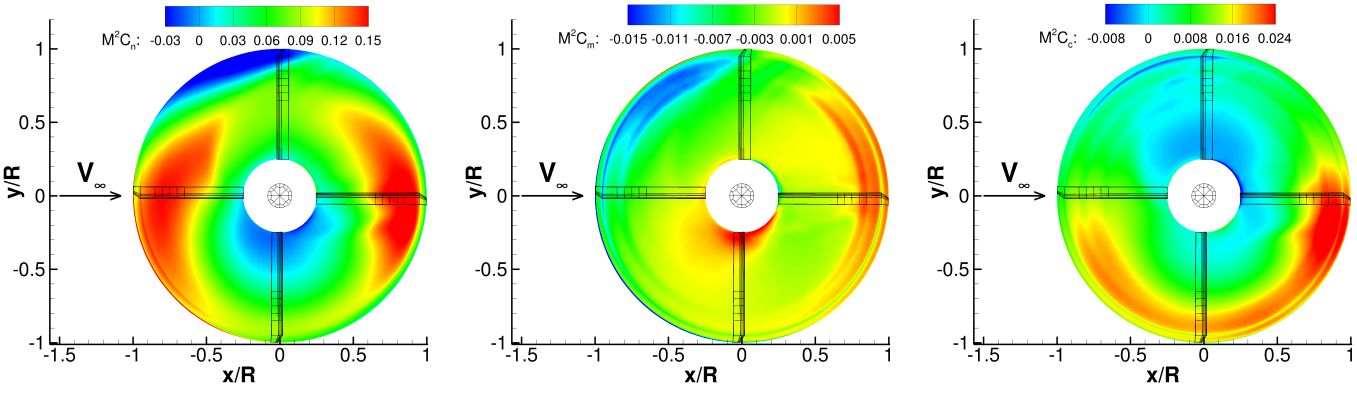


(g) PSP, $M^2C_N$ (h) PSP, $M^2C_M$ (i) PSP, $M^2C_C$

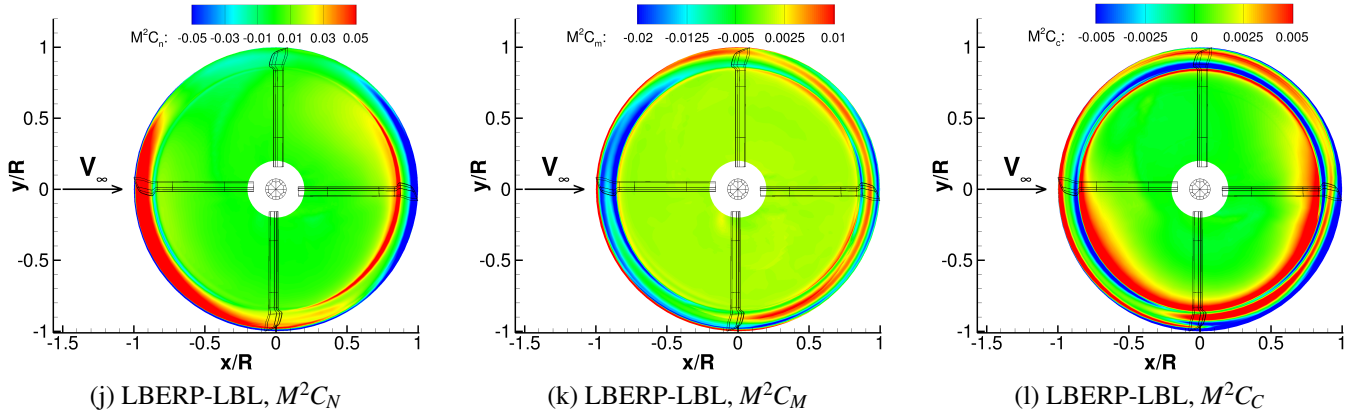


(j) LBERP-LBL, $M^2C_N$ (k) LBERP-LBL, $M^2C_M$ (l) LBERP-LBL, $M^2C_C$

**Fig. 18. Rotor disk plane load distributions for LBERP, LBL and PSP blades at $C_T = 0.0081, \mu = 0.4$. All loads are scaled by the reference blade chord, equal to the chord of the first aerodynamic section.**

Figure 18 indicates fairly similar load distributions for the three blade designs. Unfortunately, the loads from the PSP case, cannot be compared quantitavely with the Langley blades due to the lower blade tip Mach number. However, qualitatively, the normal force distributions indicate that the main lifting regions are the front and back of the rotor disk. The LBERP blade, provides a higher normal force at the front of the rotor disk and on the retreating blade, when compared to the LBL blade, which is not surprising due to the tip shape (larger chord). On the advancing blade a slightly larger region of negative thrust can be seen. The extent of this region is significantly increased for the PSP rotor blade. This is predominantly, due to the higher twist of this rotor blade, leading to operation of the local aerofoil section in this region at higher negative angles of incidence. The moment distributions indicate a positive, nose-up pitching moment as the blade moves from the back of the disk to the advancing side and a nose-down negative pitching moment as the blade moves from the advancing side to front of the disk. The LBERP blade exhibits much larger pitching moments compared to the simpler LBL and PSP planforms. In particular, the moments indicate, blade structural untwisting across the blade tip at the advancing side and increased twisting on the retreating side. This could have positive effects on the rotor performance, however, as the blade is modelled as rigid, structural deformations are not taken into account. Regarding the chordwise force distribution, for all three rotor blades, the high regions of torque are at the front and back of the rotor disk as well as the retreating side. On the advancing side, the notch feature of the LBERP planform and the initiation of the sweep for the PSP rotor blade, lead to a negative chordwise force. A similar effect is seen for the LBL blade, in the position of the aerofoil transition region to a lesser degree. The LBERP blade produce a significantly higher torque inboards of the blade tip compared to the LBL blade. This is due to the higher loading close to the notch feature of the LBERP planform. Significant variations can be seen across the blade tip which generally follow the pitching moments distribution. A nose-up pitching moment generally leads to an increase in the local chordwise force. Based on the blade load distributions, it can be stated, that aeroelastic deflections will be important for simulation of advanced planforms, as a much larger variation of pitching moments is seen across the rotor blade tip, leading to much more significant elastic blade twist deformations. The blade loads are compared quantitavely for the LBL and LBERP blades, by extracting the azimuthal loads at r/R = 0.75, 0.9 and 0.975 which is shown in figure 19

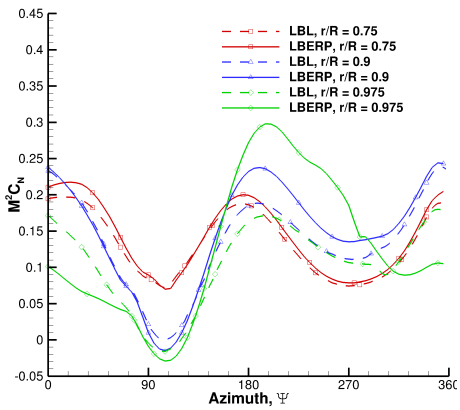


(a) Normal force

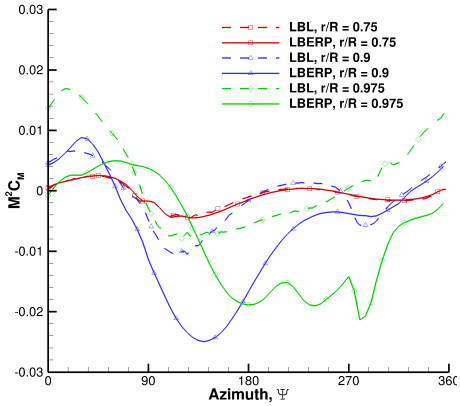


(b) Pitching moment

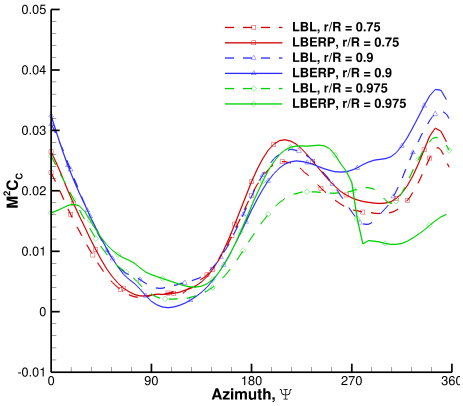


(c) Chordwise force

**Fig. 19. Azimuthal blade loads for the LBERP and LBL blades. Loads are normalised by the reference blade chord (chord of the first aerodynamic section).**

As expected, at the r/R=0.75 radial station, the loads for the Langley BERP and Baseline blades are very similar, as the shape of the planform and aerofoil sections are the same. The effect of the notch can be seen at this station in the slightly higher normal and chordwise forces at the front and back of the rotor disk. At the r/R=0.9 radial station, the Langley BERP blade starts to lift more at the back of the disk at the expense of high nose-down pitching moment on the advancing blade side and higher torque on the retreating blade side. A higher chordwise force is also encountered on the retreating blade. At r/R=0.975 the Langley BERP blade obtains much higher normal force can be seen at the back of the disk, however, on the retreating side a loss of lift is encountered leading to a normal force and chordwise force reduction at the front of the disk. A certain level of oscillations exist in the pitching moment curve at r/R = 0.975 for the LBERP blade.

The advancing and retreating blade sides are examined in more detail for all three blade designs. The surface pressure coefficient distributions at $90^o$ azimuth can be seen in figure

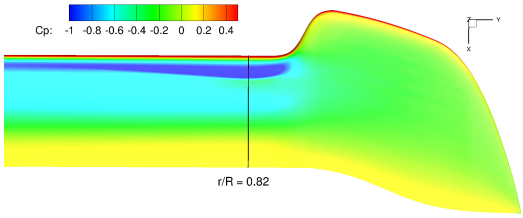


(a) LBERP

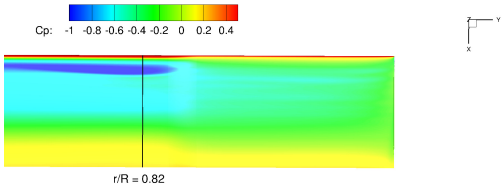


(b) LBL

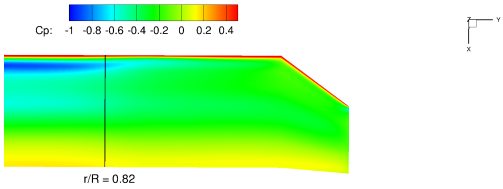


(c) PSP

**Fig. 20. Advancing side pressure distributions for the LBERP, LBL and PSP rotor blades at $\mu = 0.4, C_T = 0.0081$.**

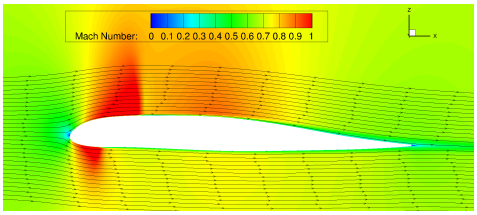


(a) LBERP

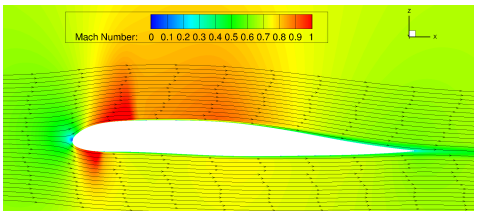


(b) LBL

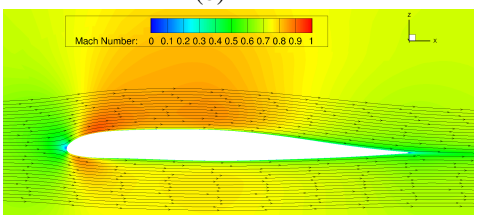


(c) PSP

**Fig. 21. Flow field streamlines and contours of Mach number at r/R = 0.82 and $90^o$ azimuth for LBERP, LBL and PSP blade designs in high-speed forward flight $\mu = 0.4, C_T = 0.0081$.**

The surface pressure solutions on the advancing blades indicate strong shocks for both LBERP and LBL blade. The notch geometry prevents the shock from propagating onto the tip surface through a reduction in the thickness/chord ratio. However, it can be seen that for the rectangular LBL blade, the shock also stops at a similar radial location. This is the position of the aerofoil transition (r/R=0.84-r/R=0.866). Another geometric design feature that may have a significant effect on the dissipation of the shock is the sudden change in the gradient of the blade twist curve. The twist is constant across both the LBL and LBERP blade tips, which generates an aerodynamic discontinuity at r/R = 0.866. Based on these observations, it is not surprising that both blades show similar values of normal and chordwise forces on the advancing blade side. The strong nose-down pitching moment for the LBERP blade, however, could give rise to significant pitch-link loads. The addition of blade anhedral could potentially reduce these strong pitching moment variations. The PSP blade surface pressure distribution indicates, that the region of high suction is reduced more gradually, as a shock does not form. This is expected due to the lower blade tip Mach number compared to the other two blades. The nature of the shock on the advancing blade is examined in more detail by extracting the flow field streamlines and Mach number contours at r/R = 0.82 for the three blade designs, shown in figure 21.

The Mach number contours, show a larger chordwise extent of supersonic flow for the LBERP blade compared to the LBL design. The primary reason for this is associated with the higher net thrust produced by the LBERP blade, leading to a stronger downwash field near the blade tip. A weaker shock also forms on the blade lower surface for both Langley blade designs. No evidence of shock-induced separation is seen on the blade upper surface for either blade design, with a small recirculation bubble present on the blade lower surface for the LBL and LBERP blades. The PSP Mach contours only indicate the presence of the compression on both upper and lower surface, without the presence of a distinct shockwave, which is due to the lower blade tip Mach number. The retreating side flow physics are also examined in more detail. The surface pressure coefficient distributions based on local flow velocity near the blade tip are shown in figure 22, whereas the surface skin friction lines and skin friction coefficient distributions are shown in figure 23.

No evidence of dynamic stall was found for any of the blade designs in the high-speed forward flight condition. The loading distribution on the retreating side for the LBERP blade indicates the presence of a notch vortex which prevents propagation of separated flow to the blade tip. Due to the moderate thrust coefficient, no significant separation is seen inboard of the notch and as expected the flow over the blade tip remains attached. At the very tip of the LBERP blade, changes can be seen in both the pressure distributions and skin friction lines. The tip vortex rolls up on the upper surface of the blade inboards of the very tip of the blade up to the $270^o$ azimuthal location. After passing the retreating side, a drop in skin friction can be observed, along with the skin friction

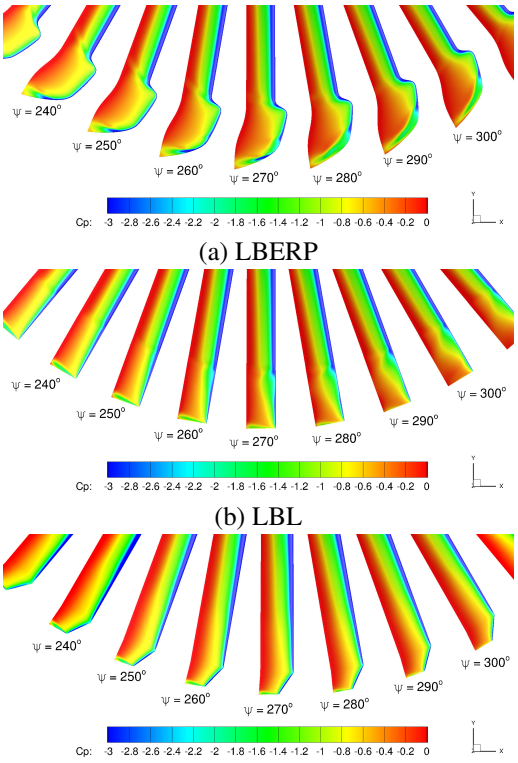


(a) LBERP

(b) LBL

(c) PSP

**Fig. 22. Retreating side pressure distributions for the LBERP, LBL and PSP rotor blades.**

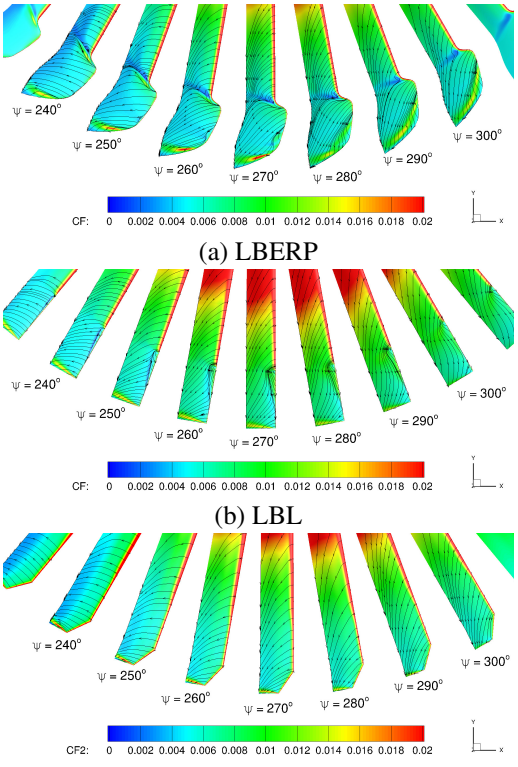


(a) LBERP

(b) LBL

(c) PSP

**Fig. 23. Retreating side skin friction lines and skin friction coefficient distributions for the LBERP, LBL and PSP rotor blades.**

lines oriented in a more spanwise direction. Here, the tip vortex rolls up around the curved blade tip and detaches further outboard. Once again, the thickness distribution across the very blade tip of this geometry could have a significant effect on the flow physics in this region. The surface pressure distributions for the LBL blade shows a distinct drop in the suction pressure in the aerofoil transition region. As indicated by the skin friction lines, a separation bubble is present near the leading edge of the blade. The chordwise extent of this separation, however, is not very large, hence not leading to a drastic increase in the rotor power. While, the steep reduction in aerofoil thickness and discontinuity in the blade twist led to promising features for the LBL blade on the advancing blade side, adverse flow features were found on the retreating side. However, these features would have a much more significant effect, if the LBL blade was simulated at the same geometric solidity as the LBERP blade, leading to more severe retreating side separation, and potentially dynamic stall. No flow features of major significance, can be seen for the PSP rotor blade design showing that this rotor does not suffer from poor retreating blade performance due to the low blade tip Mach number. At a higher thrust level (or matched net thrust), however, this blade may stall more abruptly compared to the Langley blade designs due to lower blade tip area and lower tip speed.

## CONCLUSIONS

The current CFD method, provided good hover and high-speed forward flight performance predictions for the Langley Baseline and BERP blades when compared with experimental data (Ref. 4). The validation efforts were further supported by good agreement of the surface pressure distributions with experimental data for the PSP rotor blade. Nevertheless, the available experimental data and accuracy for advanced blade validation is not at the level required by modern CFD methods. New test data is required to fully validate novel blade planforms, including a more comprehensive dataset than just integrated loads.

The design analysis section, proved that typically used efficiency metrics such as Figure of Merit and Lift to Drag ratio are only valid when comparing rotors at the same disk loading and operating conditions. When comparing rotors at different tip speeds, radii and geometric solidities, operating in dimensional units such as net thrust and net power provides more insight than in non-dimensional coefficients. Further comparison of the three blade designs should be performed trimmed to the same rotor net thrust.

The qualitative comparison of the LBERP, LBL and PSP blade designs showed that advanced planforms require computational optimisation. Geometric features such as the notch geometry, paddle-type swept tip shape and blade thickness distribution are seen to have a major impact on flow features around the complex blade tip, leading to changes in the blade loading distribution, and hence rotor performance.

## ACKNOWLEDGMENTS

This work is funded by DSTL (Defence Science and Technology Laboratory), Project No. 74260. A part of the technical work has been completed under the collaboration project, TTCP AER CP13.A1, Next Generation Rotor Blade Design. This work used the Cirrus UK National Tier-2 HPC Service at EPCC (http://www.cirrus.ac.uk). This work used the ARCHER UK National Supercomputing Service (http://www.archer.ac.uk). This work is dedicated to the memory of J. F. Perry, Chief Aerodynamicist of Westland Helicopters and BERP Technology Pioneer, who passed away in February 2019.

## REFERENCES

[1]Perry, F., "Aerodynamics of the World Speed Record," *43rd Annual Forum of the American Helicopter Society*, 1987.

[2]Rauch, P., Gervais, M., Cranga, P., Baud, A., Hirsch, J., Walter, A., and Beaumier, P., "Blue Edge (TM): The Design, Development and Testing of a New Blade Concept," *American Helicopter Society 67th Annual Forum*, 2011.

[3]Boeing, "New Chinook Composite Blades Proven," `http://www.boeing.com/features/2017/01/chinook-blades-01-17.page`, 2017, [Online; accessed 22-March-2018].

[4]Yeager Jr, W., Noonan, K., Singleton, J., Wilbur, M., and Mirick, P., "Performance and Vibratory Loads Data From a Wind-Tunnel Test of a Model Helicopter Main-Rotor Blade With a Paddle-Type Tip," Tech. rep., 1997, NASA-TM-4754.

[5]Wong, O., Watkins, A., Goodman, K., Crafton, J., Forlines, A., Goss, L., Gregory, J., and Juliano, T., "Blade Tip Pressure Measurements using Pressure Sensitive Paint," *American Helicopter Society 68th Annual Forum*, 2012.

[6]Steijl, R., Barakos, G. N., and Badcock, K., "A framework for CFD analysis of helicopter rotors in hover and forward flight," *International Journal for Numerical Methods in Fluids*, Vol. 51, No. 8, 2006, pp. 819–847, DOI: 10.1002/d.1086.

[7]Steijl, R. and Barakos, G. N., "Sliding mesh algorithm for CFD analysis of helicopter rotor-fuselage aerodynamics," *International Journal for Numerical Methods in Fluids*, Vol. 58, No. 5, 2008, pp. 527–549, DOI: 10.1002/d.1757.

[8]Osher, S. and Chakravarthy, S., "Upwind schemes and boundary conditions with applications to Euler equations in general geometries," *Journal of Computational Physics*, Vol. 50, No. 3, 1983, pp. 447–481, DOI: 10.1016/0021-9991(83)90106-7.

[9]van Leer, B., "Towards the ultimate conservative difference scheme. V.A second-order sequel to Godunov's Method," *Journal of Computational Physics*, Vol. 32, No. 1, 1979, pp. 101–136, DOI: 10.1016/0021-9991(79)90145-1.

[10]van Albada, G. D., van Leer, B., and Roberts, W. W., "A Comparative Study of Computational Methods in Cosmic Gas Dynamics," *Astronomy and Astrophysics*, Vol. 108, No. 1, 1982, pp. 76–84.

[11]Axelsson, O., *Iterative Solution Methods*, Cambridge University Press: Cambridge, MA, 1994.

[12]Woodgate, M. and Barakos, G., "An Implicit Hybrid Method for the Computation of Rotorcraft Aerodynamic Flows," *AIAA SciTech Forum, 54th Aerospace Sciences Meeting*, 2016.

[13]Noonan, K. W., "Aerodynamic Characteristics of Two Rotorcraft Airfoils Designed for Application to the Inboard Region of a Main Rotor Blade," NASA TP-3009, U.S. Army Aviation Systems Command, TR-90-B-005, July 1990.

[14]Noonan, K. W., "Aerodynamic Characteristics of a Rotorcraft Airfoil Designed for the Tip Region fo a Main Rotor Blade," NASA TM-4264, U.S. Army Aviation Systems Command, TR-91-B-003, May 1991.

[15]Amer, K., "Technical Note: High Speed Rotor Aerodynamics," *Journal of American Helicopter Society*, Vol. 34, No. 1, 1989, pp. 63–63.

[16]Perry, F., "Technical Note: The Contribution of Planform Area to the Performance of the BERP Rotor (Reply to Kenneth B. Amer)," *Journal of American Helicopter Society*, Vol. 34, No. 1, 1989, pp. 64–65.

[17]Overmeyer, A. D. and and, P. B. M., "Measured Boundary Layer Transition and Rotor Hover Performance at Model Scale," *Proceedings of the 55th Aerospace Sciences Meeting*, AIAA-2017-1872, Grapevine, Texas, 2017, pp. 1–36.

[18]Rohit, J., "CFD Performance and Turbulence Transition Predictions on an Installed Model-scale Rotor in Hover," *Proceedings of the 55th Aerospace Sciences Meeting*, AIAA-2017-1871, Grapevine, Texas, 2017, pp. 1–29.

[19]Fitzgibbon, T., Jimenez-Garcia, A., Woodgate, M., and Barakos, G., "Numerical Simulation of Different Rotor Designs in Hover and Forward Flight," *44th European Rotorcraft Forum*, 2018.

[20]Le Pape, A. and Beaumier, P., "Numerical Optimization of Helicopter Rotor Aerodynamic Performance in Hover," *29th European Rotorcraft Forum*, 2003.

[21]Dumont, A., Le Pape, A., Peter, J., and Huberson, S., "Aerodynamic Shape Optimization of Hovering Rotors Using a Discrete Adjoint of the Reynolds-Averaged Navier-Stokes Equations," *American Helicopter Society 65th Annual Forum*, 2009.

[22]Leon, E., Le Pape, A., Desideri, J., Alfano, D., and Costes, M., "Concurrent Aerodynamic Optimization of Rotor Blades Using a Nash Game Method," *69th Annual Forum of the American Helicopter Society*, 2013.

[23]Imiela, M., "High-fidelity optimization framework for helicopter rotors," *Journal of Aerospace Science and Technology*, Vol. 23, No. 1, 2012, pp. 2–16.

[24]Robinson, K. and Brocklehurst, A., "BERP IV Aerodynamics, Performance and Flight Envelope," *34th European Rotorcraft Forum*, 2008.

[25]Balch, D. and J.Lombardi, "Experimental Study of Main Rotor Tip Geometry and Tail Rotor Interactions in Hover, Vol I - Text and Figures," Tech. rep., National Aeronautics and Space Administration, 1985, NASA-CR-177336-Vol-1.

[26]Brocklehurst, A. and Barakos, G., "A review of helicopter rotor blade tip shapes," *Progress in Aerospace Sciences*, Vol. 56, 2013, pp. 35 – 74.